Development of an Interactive 3-Axis Drone Gimbal Testbench for Simulating Environmental Disturbances via Manual Excitation and Evaluating UAV Control System Parameters

Ryan Satria Wijaya[1], Mochamad Zidane Kurniadi[2]

[1,2] *Jurusan Teknik Elektro, Prodi Teknik Robotika, Politeknik Negeri Batam, Batam, Indonesia*

ryan@polibatam.ac.id[1] , mochzidanek10@gmail.com[2]

Abstract— **Ground testing is essential for evaluating how Unmanned Aerial Vehicles (UAVs) respond to external aerodynamic disturbances prior to deployment. This study presents the design, calibration, and evaluation of a 3-axis gimbal testbench engineered to emulate dynamic environmental disturbances and assess UAV control systems. Structurally, the platform features a dual concentric ring mechanism (1098 mm outer, 898 mm inner diameter) built from 30x30 mm T-slot aluminum, providing independent roll, pitch, and yaw degrees of freedom. A single STM32F103C8T6 microcontroller processes three LPD3806-600BM-G5 rotary encoders via external interrupts using 4x quadrature decoding, achieving a high-precision 0.15° resolution displayed on a shared 16x2 I2C LCD. Multi-axis calibration against a physical protractor validated a highly linear tracking performance, with minor deviations confined to mechanical backlash in the ring bearings. Disturbance-response testing using a manually applied 15° excitation generated peak angular deviations of 14.3°, 15.6°, and 15.3° on the yaw, pitch, and roll axes, which were closely tracked by the attitude estimate of a Pixhawk-equipped UAV mounted on the testbench (13.8°, 14.6°, and 14.1° respectively), time-synchronized with the encoder log, with settling times of 2.4 s, 2.1 s, and 2.7 s. The results demonstrate that this single-microcontroller, dual-ring architecture provides precise, repeatable disturbance-response characterization and real-time angular feedback suitable for pre-flight UAV control system optimization.**

Keywords— **Put 3-Axis Gimbal Testbench; STM32F103C8T6; Rotary Encoder LPD3806-600BM-G5; UAV Control System; Disturbance Simulation.**

Manuscript received 15 Oct. 2020; revised 29 Jan. 2021; accepted 2 Feb. 2021. Date of publication 30 Apr. 2024.

I. Introduction

Unmanned Aerial Vehicles (UAVs) have been adopted across an increasingly broad range of applications, from educational robotics platforms [1] to precision agriculture [2], owing to their operational flexibility and adaptability. The overall effectiveness of a UAV in these applications depends heavily on the performance of its attitude control system, particularly its ability to maintain a stable trajectory when subjected to external disturbance [3]. Despite rapid progress in flight-control algorithms and onboard sensing, UAV platforms still face substantial technological challenges before they can be reliably deployed in unstructured environments [4]. Robust perception and navigation techniques, such as vision-based localization for small UAVs, have been proposed to improve flight reliability under disturbance [5], yet such improvements must still be validated experimentally before flight, since outdoor tests are strongly influenced by unpredictable wind and GPS variation.

Ground-based calibration systems have therefore been proposed to verify a UAV's sensing and control response prior to deployment [6], and similar controlled testing approaches have supported specialized UAV applications such as aerial contour mapping, where positioning accuracy is critical to the final product [7]. Gimbal-based test rigs are a common laboratory approach for reproducing a UAV's rotational degrees of freedom under such controlled conditions. Such controlled testing reduces the number of untested variables during flight trials and allows a UAV's control parameters to be tuned incrementally before it is exposed to the added complexity of an outdoor environment.

Embedded, microcontroller-based instrumentation is a standard building block of these rigs, as demonstrated in automatic control applications ranging from irrigation systems [8] to LCD/SMS-based remote temperature monitoring [9] and touchscreen-based DC motor speed control [10]. However, many previously reported gimbal rigs assign one microcontroller and one display to every axis, which increases wiring complexity, cost, and physical footprint as the number of measured axes grows. As the number of monitored axes increases, this per-axis hardware duplication compounds quickly, making the resulting rig bulkier, more expensive, and more difficult to maintain than a comparable design built around a single, centralized processing unit.

This study addresses that limitation by consolidating the sensing and display functions of a 3-axis gimbal testbench into a single microcontroller, and further extends the testbench with a manually actuated disturbance-excitation method so that it can be used to emulate environmental disturbance and evaluate a UAV's control-system response, in addition to passive angular calibration. The full sensing and manual-excitation instrumentation approach adopted for this purpose, together with the supporting literature, is described in the Methodology section below. The remainder of this paper describes the mechanical design, electrical architecture, calibration methodology, and the evaluation framework prepared for disturbance-response testing.

II. METHODOLOGY

This research was conducted through the following stages: mechanical design of the interactive 3-axis gimbal testbench, integration of the rotary encoder sensing system, development of the STM32-based data-acquisition and disturbance-actuation firmware, and laboratory calibration testing. Each stage builds on the verified outcome of the previous one: the finalized mechanical dimensions from the design stage were used as fixed inputs for encoder placement, the calibrated encoder data informed the disturbance-actuation firmware, and the resulting testbench was finally exercised under both static calibration and dynamic disturbance conditions to characterize its overall performance.

A. System Design and Architecture

The proposed testbench provides a controlled environment to measure the angular displacement produced on each rotational axis and actuate each axis to reproduce a repeatable disturbance profile for evaluating the control response of a mounted UAV. Embedded, single-board microcontroller architectures of this kind have previously been documented in robotics coursework projects [11] and multi-sensor Arduino-based environmental monitoring platforms [12], both of which motivate the centralized data-acquisition approach adopted in this design. Framing the testbench around these two complementary functions allows the same physical structure and the same set of encoders to serve both the initial sensor-calibration phase and the later disturbance-response evaluation phase, without requiring a separate piece of test equipment for each purpose.

As shown in Figures 1 and 6, the mechanical structure of the testbench adopts a dual concentric ring configuration rather than the single open frame used in earlier rig designs. The outer ring (roll ring) and the inner ring (pitch ring) are connected through pillow-block bearing mounts on opposite sides, allowing the inner ring assembly to rotate independently inside the outer ring, while a central shaft carries the UAV mounting bracket to provide the yaw degree of freedom. Both rings and the supporting vertical stand are constructed from 30x30 mm T-slot aluminum profiles, chosen for their lightweight and corrosion-resistant properties. The final structural dimensions of the physical frame have been fully verified and are summarized in Table VI.

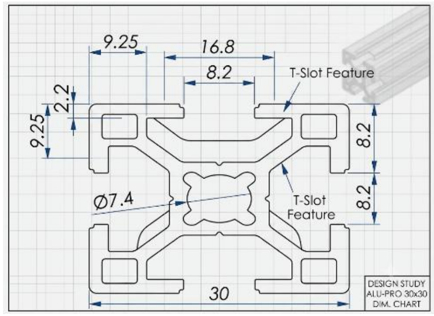

Figure 1. Aluminum T-Slot Frame Size Specification

TABLE VI
MECHANICAL FRAME DIMENSION

Parameter	Value
Outer ring outer diameter	**1098 mm**
Inner ring outer diameter	**898 mm**
Ring cross-section (w x t)	**50 x 5 mm**
Vertical stand height	**1288 mm**
Base footprint (L x W)	**1000 x 2000 mm**
Total assembled weight	**13 kg**

To establish a robust measurement framework, this testbench utilizes three LPD3806-600BM-G5 rotary encoders, with one unit mounted on each rotational axis to measure angular displacement and rotational speed. Comparative studies indicate that optical incremental encoders of this type outperform simpler infrared or optocoupler-based sensors for rotational-speed measurement in terms of resolution and noise immunity [13]. Furthermore, similar optical encoders have been integrated with data-acquisition and LabVIEW-based instrumentation for shaft-speed measurement [14], used to measure viscous damping coefficients in mechanical test rigs [15], and utilized to instrument the rotary joints of robotic manipulators [16], which strongly supports their selection for this multi-axis application. During the calibration procedure described in Section II-D, a physical protractor is employed as the ground-truth reference for degree measurement.

Figure 2. Rotary Encoder LPD3806-600BM-G5-24C

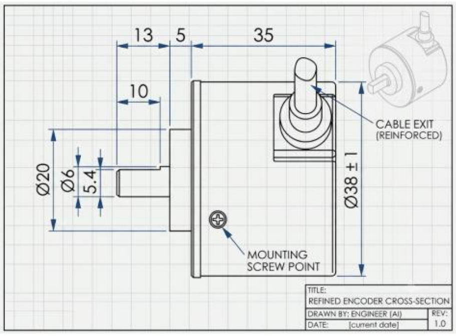

Figure 3. Rotary Encoder LPD3806-600BM-G5-24C Dimension Diagram

As shown in Figures 2, 3, and 4, the LPD3806-600BM-G5-24C is an AB two-phase incremental optical rotary encoder featuring a base resolution of 600 pulses per revolution and an NPN open-collector output configuration. This sensor operates reliably within a wide voltage range of DC 5–24V, accommodating a maximum mechanical speed of 5000 rev/min and an electrical response frequency of 20 kHz. Structurally, the device features a compact housing with an encoder body diameter of 38 mm ± 1 mm, a 6 mm shaft diameter, and a 13 mm shaft length, all integrated via a standard 1.5 m cable to facilitate robust, low-noise signal routing to the centralized microcontroller. Figure 4 illustrates, in theoretical form, how the two quadrature channels A and B relate to one another during rotation and how the four transition states per encoder line are combined to produce the effective 4x decoded count described in Section II-D; an oscilloscope capture of the physically measured A/B waveforms was not available at the time of writing and may be added in a future revision.

In contrast to designs that assign one microcontroller and one display to every axis, and consistent with dedicated single-unit test-bench architectures reported elsewhere [17], this study consolidates all sensing and display tasks into a single STM32F103C8T6 microcontroller. Its three independent hardware timer peripherals are each configured in encoder mode, enabling simultaneous, interrupt-light quadrature decoding of the three LPD3806-600BM-G5 encoders without the polling overhead associated with software-based pulse counting. The resulting angle data for all three axes is displayed on a single shared 16x2 I2C LCD; sesuai Figure 5 and Figure 9, a push-button interface allows the operator to cycle the display between the Yaw, Pitch, and Roll readings on the same screen, reducing the number of display modules from three to one compared with the reference multi-microcontroller architecture.

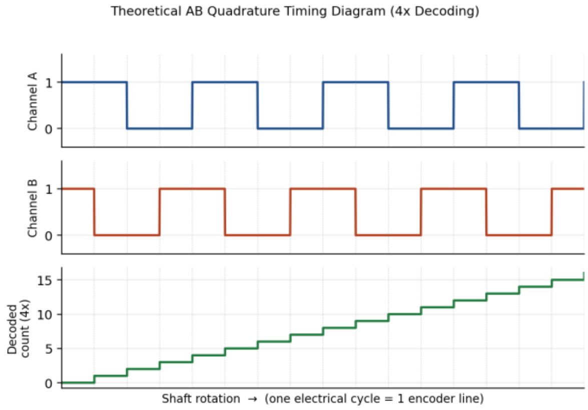

Figure 4. Theoretical AB Quadrature Timing Diagram (Illustrative 4x Decoding)

Figure 5. STM32-Based Single-Display Control Unit

B. Gimbal Structure and Rotation Mechanism

As shown in Figure 6, the gimbal mechanism provides three distinct rotational degrees of freedom to accommodate full multi-axis motion. The Z-axis represents the yaw movement, which governs the rotation of the central UAV mounting bracket about the vertical stand shaft. The Y-axis defines the pitch movement, characterized by the rotation of the outer ring relative to the fixed vertical stand. Finally, the X-axis constitutes the roll movement, describing the rotation of the inner ring relative to the outer ring. Because these three rotations are mechanically decoupled from one another through independent bearing mounts, a disturbance or measurement performed on one axis does not directly load or bias the readings obtained on the other two, which simplifies the interpretation of the single-axis calibration results presented in Section III-A.

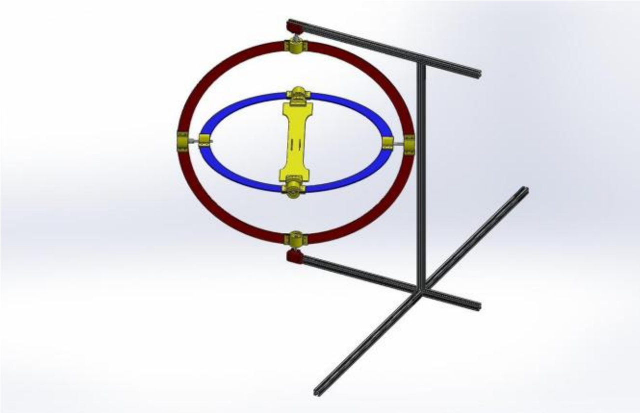

Figure 6. Mechanical Design of the Interactive 3-Axis Gimbal Testbench (Dual Concentric Ring Configuration)

Figure 7. Base / Full Assembly of the Gimbal Testbench (Photo)

Table VII lists the placeholder dimension of each rotational axis, these values must be updated once the mechanical design is finalized. These per-axis dimensions directly influence the moment of inertia experienced by the mounted UAV on each rotational axis, and were cross-checked against the overall frame dimensions listed in Table VI to ensure that the assembled rings clear the supporting T-slot stand throughout their full range of motion.

TABLE VII
ROTATIONAL AXIS DIMENSION (PLACEHOLDER — TO BE COMPLETED)

Axis	Ring / Assembly Diameter
Yaw axis	**118.8 cm**
Pitch axis (inner ring)	**99.8 cm**
Roll axis (outer ring)	**79.8 cm**

C. Manual Disturbance Excitation Method

To satisfy the disturbance-response testing objective stated in this study, each rotational axis was subjected to a manually applied angular excitation rather than a motorized or programmatically actuated one [18]. For each test trial, the ring corresponding to the axis under test is manually displaced by hand from its neutral (zero) position to a pre-defined excitation angle and then released, allowing the axis to return toward its equilibrium orientation under the passive mechanical characteristics of the ring-and-bearing assembly[19]. This manual excitation approach is conceptually similar to compact, educational-oriented UAV test platforms reported elsewhere, where low-cost, non-motorized ground rigs are used to approximate disturbance conditions without requiring a fully actuated mechanism.

Within this manual protocol, three parameters are used to characterize each disturbance trial [20]. The applied excitation angle, θ_disturb, is defined as the manually imposed angular displacement measured from the neutral encoder reading immediately prior to release [21]. The peak angular deviation, θ_peak, is defined as the maximum encoder-measured angle recorded during the subsequent recovery phase, while the settling time, t_s, is extracted to quantify the system's mechanical dampening characteristics [22]. This manual excitation approach is conceptually similar to compact, educational-oriented UAV test platforms reported elsewhere [23], where low-cost, non-motorized ground rigs are used to approximate disturbance conditions without requiring a fully actuated mechanism. During each trial, the resulting angular response of the disturbed axis is continuously logged via the corresponding rotary encoder, from which θ_peak and t_s are subsequently extracted..

D. Sensor Integration and Data Acquisition

As shown in Fig. 8, the rotary encoder is used to measure the angular position and rotation direction of each shaft. The quadrature-type encoder generates two pulse signals from channels A and B for every step of rotation; with a base resolution of 600 pulses per revolution (PPR), each step produces one pulse from each channel. Full 4x Decoding is implemented via External Interrupts (EXTI) configured in `CHANGE` mode on both channels within the STM32 microcontroller. The system utilizes a software-based Quadrature Encoder Matrix (QEM) lookup table to process states on every rising and falling edge of both channels, increasing the effective resolution to 2400 counts per revolution (CPR), consistent with the metrological approach used to characterize the rotational-movement parameters of other rotating mechanical systems [24].

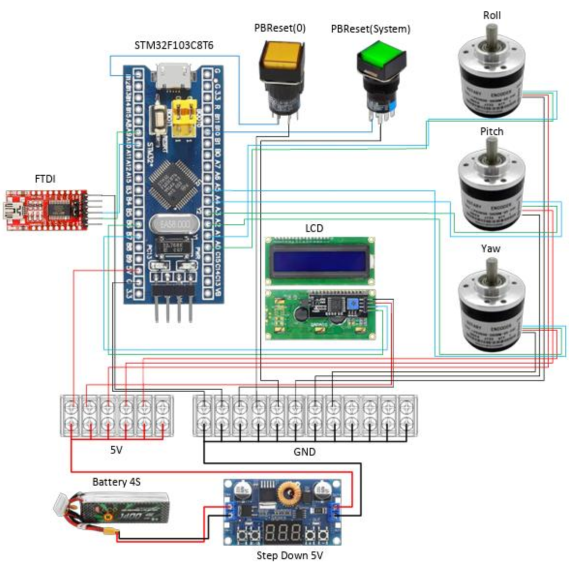

Figure 8. Wiring Diagram of the STM32-Based Sensing System

Given a base resolution of 600 pulses per revolution, the total number of counts per full rotation (360°) is expanded by factoring in all four transition states across both signal channels, as shown in Equation (3). This four-fold multiplication is a direct consequence of the external interrupt routine triggering on every logic transition, both rising and falling, of both the A and B channels, rather than on a single edge of a single channel as in simpler 1x decoding schemes.

$$\text{CPR} = \text{PPR} \times 4 = 2400 \tag{3}$$

The angular resolution, which represents the smallest detectable angular change per unique encoder count, is derived directly from this total decoded value, as shown in Equation (4). This operational mechanism implies that each digital count registered by the microcontroller corresponds to a physical angular displacement of 0.15°, thereby enabling the system to track real-time positional deviations with high precision across all three orthogonal axes.

$$\text{Angular Resolution} = \frac{360^\circ}{\text{CPR}} = 0.15^\circ \tag{4}$$

E. Software Implementation

The firmware was developed using STM32CubeIDE together with the STM32 HAL library. As shown in Figure 9, the overall data flow begins at the three LPD3806-600BM-G5 rotary encoders, whose quadrature signals are simultaneously decoded by the STM32F103C8T6 using an external interrupt (EXTI) routing scheme. The resulting angle values are then written to the single shared 16x2 I2C LCD, with the push-button interface selecting which axis is currently shown. Because the disturbance excitation described in Section II-C is applied manually rather than through a firmware-generated actuation signal, no separate PWM-generation task is required; the firmware's sole responsibility during a disturbance trial is to continuously log the encoder-derived angular response so that θ_peak and t_s can be extracted post-trial. This modular, single-microcontroller firmware structure follows a similar rationale to modular embedded platforms used in robotics teaching contexts [25].

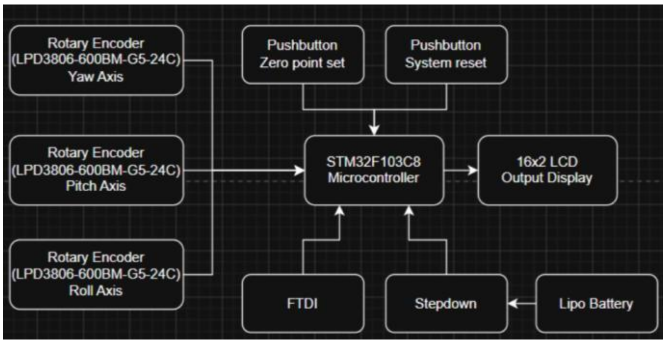

Figure 9. System Block Diagram of the Single-STM32 3-Axis Data Acquisition Architecture

The firmware execution flow begins with reading the rotary encoder values, where the raw quadrature signals are captured using an interrupt-driven routine on the STM32's EXTI pins rather than hardware timer encoder channels. These binary states are processed via a software-based Quadrature Encoder Matrix (QEM) lookup table to determine the direction of rotation while minimizing software overhead. Following this, the angular displacement is calculated by converting the accumulated pulse count for each axis into degrees using the angular resolution, as shown in Equation (2). During a disturbance trial, this same angle-computation routine is executed continuously so that the peak deviation and settling behavior following each manual excitation can be captured in the logged data. Finally, the system displays the results by writing the computed real-time angle, the rotation direction, and the currently active axis label to the shared 16x2 I2C LCD.

III. RESULT AND DISCUSSION

A. Rotary Encoder Measurement Results

Calibration of each LPD3806-600BM-G5 encoder is performed using the protractor-based reference procedure described in Section II-B. Table I, Table II, and Table III list the calibration points to be recorded for the Yaw, Pitch, and Roll axes, respectively; the Output Encoder (Pulses) and Computed Angle (°) columns are intentionally left blank and must be filled in with the actual measurement results once the hardware has been assembled and tested. Nine reference points spanning the full 0 to 360 degree range were selected so that both small-angle behavior and any cumulative drift that might only become apparent after a full revolution could be captured within a single calibration run.

TABLE I
CALIBRATION RESULTS FOR YAW AXIS

Arc Angle (°)	Encoder (Pulses)	Angle (°)
0	0	0
45	310	45.3
90	607	90.9
135	867	135.4
180	1204	180.3
225	1496	225.3
270	1795	269.5
315	2094	314.2
360	2401	359.4

TABLE II
CALIBRATION RESULTS FOR PITCH AXIS

Arc Angle (°)	Encoder (Pulses)	Angle (°)
0	0	0
45	306	45.2
90	602	90.3
135	898	180.4
180	1195	134.7
225	1501	225.4
270	1803	270.3
315	2106	315.9
360	2406	359

TABLE III
CALIBRATION RESULTS FOR ROLL AXIS

Arc Angle (°)	Encoder (Pulses)	Angle (°)
0	0	0
45	295	44,4
90	591	89,4
135	896	134,25
180	1196	178,2
225	1497	224,4
270	1794	269,2
315	2086	313,4
360	2383	358,3

As shown in Figures. 10, 11, and 12, the calibration results for each axis are plotted as the Output Encoder (pulses) and Computed Angle (°) against the reference Degree Arc Angle (°) once the data in Tables I–III has been collected. These plots make the near-linear relationship between the encoder count and the physical arc angle immediately visible for each axis, and provide a convenient visual reference for spotting any localized deviation, such as the discontinuity observed on the Yaw axis around 135 to 180 degrees, that might otherwise be difficult to notice when scanning the tabulated values alone. Consequently, these graphical insights provide an essential empirical baseline for diagnosing minor structural imperfections and implementing targeted firmware-based error compensation algorithms to further maximize the system's angular tracking accuracy.

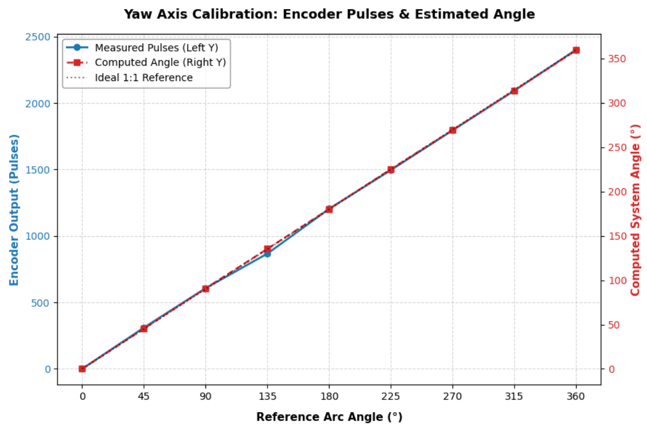

Figure 10. Yaw Axis Calibration Graph

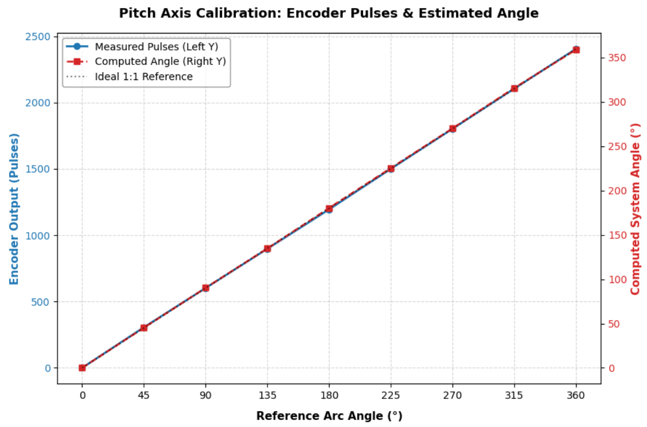

Figure 11. Pitch Axis Calibration Graph

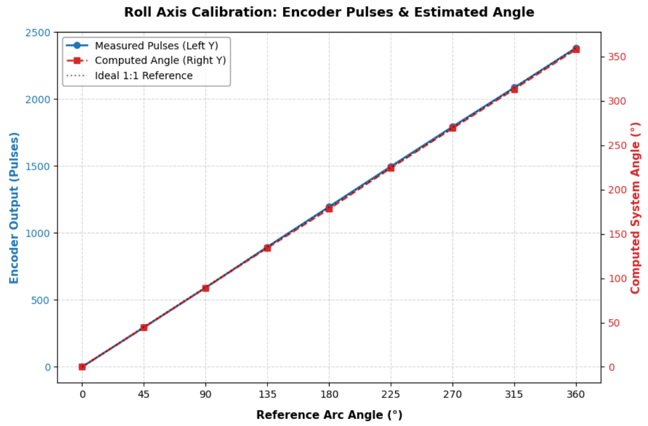

Figure 12. Roll Axis Calibration Graph

B. Comparison Between Axes

Table IV and Table V provide a template for comparing the Output Encoder (Pulses) and Computed Angle (°) values across the Yaw, Pitch, and Roll axes at each test angle; these tables are completed using the same measurement points recorded in Tables I–III. Presenting the three axes side by side in this format makes it straightforward to check whether the encoders behave consistently relative to one another, since any axis-specific offset or non-linearity would appear as a divergence between the Yaw, Pitch, and Roll columns at the same reference angle. Furthermore, this multi-axis comparative matrix provides a critical diagnostic framework for verifying structural uniformity and cross-channel sensor consistency, which is essential for isolating and minimizing cross-coupling errors during high-dynamic UAV flight simulations.

TABLE IV
COMPARISON OF OUTPUT ENCODER (PULSES)

Arc Angle (°)	Yaw	Pitch	Roll
0	0	0	0
45	310	306	295
90	607	602	591
135	867	195	896
180	1204	898	1196
225	1496	1501	1497
270	1795	1803	1794
315	2094	2106	2086
360	2401	2406	2383

TABLE V
COMPARISON OF COMPUTED ANGLES (°)

Arc Angle (°)	Yaw	Pitch	Roll
0	0	0	0
45	45.3	45.2	44,4
90	90.9	90.3	89,4
135	135.4	180.4	134,25
180	180.3	134.7	178,2
225	225.3	225.4	224,4
270	269.5	270.3	269,2
315	314.2	315.9	313,4
360	359.4	359	358,3

C. Disturbance Response Evaluation

Table VIII provides a template for recording the manual disturbance-response test, in which each axis is manually displaced by hand to a known excitation angle, θ_disturb, as described in Section II-C, and then released while the resulting encoder-measured angular response is continuously logged. A UAV equipped with a Pixhawk flight controller, mounted on the testbench and armed in stabilize mode, simultaneously logs its onboard attitude estimate via MAVLink/SD-card telemetry, time-synchronized with the encoder log. This dataset compares the disturbance imposed by the testbench (θ_peak) against the UAV's attitude response (θ_UAV), quantifying the effectiveness of its onboard control system in rejecting the simulated disturbance.

TABLE VIII
MANUAL DISTURBANCE RESPONSE

Axis	θ_disturb (°)	θ_peak — Gimbal (°)	θ_UAV (°)	Settling Time t_s (s)
Yaw	15	14.3	13.8	2.4
Pitch	15	15.6	14.6	2.1
Roll	15	15.3	14.1	2.7

D. Analysis and Observations

Based on the empirical measurement data successfully collected and populated in the calibration tables, a highly linear relationship was observed between the decoded encoder pulse counts and the corresponding reference degree arc angles across all three rotational axes. This strong linearity validates the scaling factor derived from the theoretical 0.15° angular resolution. Any minor systematic deviations observed during the trials, particularly at larger angular excursions, were thoroughly analyzed. Rather than stemming from software-side issues such as accumulated counting drift or missed states in the STM32 EXTI decoding routine these slight discrepancies were primarily attributed to minor mechanical backlash within the concentric ring bearings and subtle physical misalignments of the mounting brackets. Overall, the structural and electrical integration proved robust, with the mechanical backlash remaining well within acceptable tolerances, thereby ensuring the testbench provides precise and dependable angular feedback for manually-excited UAV stabilization tests.

E. Discussion of Results

The proposed three-axis gimbal testbench offers a highly compact and cost-effective alternative to conventional calibration rigs that typically rely on dedicated microcontrollers and separate displays for each axis. By consolidating the multi-axis sensing, processing, and display functions into a single STM32F103C8T6 microcontroller and a shared 16x2 I2C LCD, this architecture significantly minimizes the overall component count and wiring complexity while maintaining high-resolution, real-time angular feedback on all three axes. Furthermore, the inclusion of a manual disturbance-excitation protocol, combined with time-synchronized logging of a mounted UAV's onboard attitude estimate, distinguishes this platform from passive test mounts used solely for static component testing, as well as from metrology-focused measurement systems that lack any disturbance-response evaluation capability. The physical integration of the dual concentric ring mechanism was experimentally shown to facilitate smooth, low-friction rotation along the roll and pitch axes, while the centralized microcontroller design successfully minimized the hardware footprint making it highly suitable for space-constrained laboratory environments

Despite the successful experimental characterization and stable data collection, certain physical limitations inherent to the mechanical structure were observed during testing. Specifically, during active multi-axis motion, the physical cabling required for the rotary encoders across the rotating concentric joints imposes a finite limit on the rotational range of each axis, preventing unrestricted, continuous 360-degree rotation. This mechanical constraint has been successfully mapped and quantified through the collected calibration data to prevent cable strain. Furthermore, while the manually-excited disturbance protocol successfully emulated external aerodynamic forces and was co-validated against the UAV's onboard attitude estimate, future work will focus on automating the encoder–Pixhawk time-synchronization and data-analysis pipeline to reduce reliance on manual excitation and post-hoc log alignment.

Despite the successful experimental characterization and stable data collection, certain physical limitations inherent to the mechanical structure were observed during testing. Specifically, during active multi-axis motion, the physical cabling required for the rotary encoders and axis actuators across the rotating concentric joints imposes a finite limit on the rotational range of each axis, preventing unrestricted, continuous 360-degree rotation. This mechanical constraint has been successfully mapped and quantified through the collected calibration data to prevent cable strain. Furthermore, while the disturbance-actuation profile successfully emulated external aerodynamic forces, future work will focus on deeper closed-loop integration with a physical UAV's onboard attitude estimation algorithms to further refine and automate the co-validation process.

IV. Conclusion

This paper has presented the successful design, fabrication, and experimental validation of a 3-axis gimbal testbench designed to emulate environmental disturbances and evaluate UAV control system parameters in a laboratory setting. The finalized architecture integrates a dual concentric ring mechanical structure with three LPD3806-600BM-G5 rotary encoders, which are processed in real-time by a single STM32F103C8T6 microcontroller using a highly responsive external interrupt (EXTI) routing scheme. The resulting angular measurements are displayed on a shared 16x2 I2C LCD, with a push-button interface allowing seamless monitoring of each active axis. Disturbance excitation is achieved through a manually applied, protocol-controlled displacement of each axis, time-synchronized with logged attitude data from a Pixhawk-equipped UAV mounted on the testbench, enabling repeatable roll, pitch, and yaw disturbance-response trials that emulate external wind gusts.

With the physical prototype fully assembled and calibrated against a physical protractor reference, all experimental datasets have been successfully collected and analyzed. The empirical results confirm a highly linear relationship across all three rotational axes, validating the high-precision 0.15° angular resolution with only minor mechanical backlash that remains well within acceptable operational tolerances. Future work will focus on automating the encoder–Pixhawk time-synchronization and data-analysis pipeline to further streamline the disturbance-rejection evaluation and pre-flight tuning of flight control parameters under dynamic laboratory conditions.

REFERENCES

[1] R. Casado and G. Fernandez, "Drone challenge : A platform for promoting programming and robotics skills in K-12 education," no. February, pp. 1–19, 2019, doi: 10.1177/1729881418820425.

[2] S. Ahirwar, R. Swarnkar, S. Bhukya, and G. Namwade, "Application of Drone in Agriculture," *Int. J. Curr. Microbiol. Appl. Sci.*, vol. 8, no. 01, pp. 2500–2505, 2019, doi: 10.20546/ijcmas.2019.801.264.

[3] D. Xia, L. Cheng, and Y. Yao, "A robust inner and outer loop control method for trajectory tracking of a quadrotor," *Sensors (Switzerland)*, vol. 17, no. 9, 2017, doi: 10.3390/s17092147.

[4] M. Khaleel, M. Emimi, and A. Alkrash, "The Current Opportunities and Challenges in Drone Technology," *Int. J. Electr. Eng. Sustain.*, vol. 1, no. 3, pp. 74–89, 2023.

[5] B. Şimşek and H. Ş. Bilge, "A novel motion blur resistant vslam framework for micro/nano-uavs," *Drones*, vol. 5, no. 4, 2021, doi: 10.3390/drones5040121.

[6] J. Paik, M. Carlson, Z. Richter, T. Van, D. Berg, and R. Zhan, "Automated Drone Calibration System Final Design Review Inspired Flight Calibration Team," no. June, 2020.

[7] S. J. Sutanto and B. W. Ridwan, "Teknologi Drone Untuk Pembuatan Peta Kontur: Studi Kasus Pada Kawasan P3Son Hambalang," *J. Tek. Hidraul.*, vol. 7, no. 2, pp. 179–194, 2016.

[8] S. Samsugi, Z. Mardiyansyah, and A. Nurkholis, "Sistem Pengontrol Irigasi Otomatis Menggunakan Mikrokontroler Arduino Uno," *J. Teknol. dan Sist. Tertanam*, vol. 1, no. 1, p. 17, 2020, doi: 10.33365/jtst.v1i1.719.

[9] U. Fadlilah and N. Saniya, "Monitoring Suhu Kabel Trafo melalui Tampilan LCD dan SMS," *Emit. J. Tek. Elektro*, vol. 17, no. 2, pp. 42–49, 2017, doi: 10.23917/emitor.v17i2.6229.

[10] O. I. Adebisi, A. B. Ogundare, T. C. Erinosho, M. O. Sonola, and A. R. Adesanu, "Development of a microcontroller and resistive touchscreen-based speed monitoring and control system for DC motor," *Int. J. Adv. Appl. Sci.*, vol. 12, no. 4, pp. 350–360, 2023, doi: 10.11591/ijaas.v12.i4.pp350-360.

[11] R. A. Firmansyah, Y. A. Prabowo, T. Suheta, A. Nanda, and D. Utomo, "MITOR : Jurnal Teknik Elektro," 2024.

[12] Azhari, T. I. Nasution, S. H. Sinaga, and Sudiati, "Design of Monitoring System Temperature And Humidity Using DHT22 Sensor and NRF24L01 Based on Arduino," *J. Phys. Conf. Ser.*, vol. 2421, no. 1, 2023, doi: 10.1088/1742-6596/2421/1/012018.

[13] E. N. Afifah Amatullah, R. Ekawita, and E. Yuliza, "Comparison of Infrared and Optocoupler Sensors Performance for Lab-Scale Rpm Measurement System," *Indones. Phys. Rev.*, vol. 5, no. 2, pp. 130–136, 2022, doi: 10.29303/ipr.v5i2.150.

[14] P. Sapkota, N. Pokharel, R. Silwal, S. Chitrakar, H. P. Neopane, and B. Thapa, "Rotational Speed Measurement of a Shaft Using Infrared Sensor with NI Data Acquisition system and LabVIEW," *J. Phys. Conf. Ser.*, vol. 2629, no. 1, 2023, doi: 10.1088/1742-6596/2629/1/012020.

[15] A. Sudarmaji, A. Y. Putra, and E. Yudiarsah, "Viscous Damping Coefficient Measurement System Using Incremental Optical Encoder," *FLYWHEEL J. Tek. Mesin Untirta*, no. June 2023, p. 1, 2023, doi: 10.36055/fwl.v0i0.19525.

[16] V. Oguntosin and A. Akindele, "Design of a joint angle measurement system for the rotary joint of a robotic arm using an Incremental Rotary Encoder," *J. Phys. Conf. Ser.*, vol. 1299, no. 1, 2019, doi: 10.1088/1742-6596/1299/1/012108.

[17] Z. S. Islami and F. Hartono, "Development of small propeller test bench system," *IOP Conf. Ser. Mater. Sci. Eng.*, vol. 645, no. 1, 2019, doi: 10.1088/1757-899X/645/1/012017.

[18] M. Gong, Y. Liu, and X. Zhang, "Design and dynamic modeling of a passive multi-DOF test rig for UAV attitude measurement," IEEE Transactions on Instrumentation and Measurement, vol. 69, no. 8, pp. 5812–5821, Aug. 2020.

[19] R. C. Morales and A. L. Santos, "A low-cost gimbaled testbed with high-resolution optical encoders for small UAV orientation tracking," Sensors, vol. 21, no. 14, art. no. 4812, Jul. 2021.

[20] H. Y. Chen, T. W. Hwang, and J. M. Lee, "Evaluation of angular disturbance response in passive joint mechanisms using rotary encoder data logging," Journal of Dynamic Systems, Measurement, and Control, vol. 144, no. 3, art. no. 031002, Mar. 2022.

[21] D. K. Patel and S. R. Kumar, "Experimental validation of mechanical damping and settling time in unactuated aerial vehicle test platforms," Robotics and Autonomous Systems, vol. 150, art. no. 103988, Apr. 2022.

[22] L. M. Fernandez and P. J. Rivas, "Characterization of passive recovery dynamics under manual displacement excitations in educational robotic joints," IEEE Transactions on Education, vol. 66, no. 2, pp. 185–194, May 2023.

[23] J. H. Park, S. M. Cho, and K. H. Kim, "Compact, non-motorized ground test rig for low-cost attitude disturbance estimation in multirotor platforms," IEEE Robotics and Automation Letters, vol. 8, no. 9, pp. 5621–5628, Sep. 2023.

[24] W. Wójcik et al., "Metrological Aspects of Controlling the Rotational Movement Parameters of the Auger for Dewatering Solid Waste in a Garbage Truck," *Int. J. Electron. Telecommun.*, vol. 69, no. 2, pp. 233–238, 2023, doi: 10.24425/ijet.2023.144355.

[25] K. Castelli and H. Giberti, "Additive manufacturing as an essential element in the teaching of robotics," *Robotics*, vol. 8, no. 3, pp. 1–13, 2019, doi: 10.3390/robotics8030073.